nature COMMUNICATIONS

ARTICLE

Received 29 May 2016 | Accepted 22 Oct 2016 | Published 28 Nov 2016

DOI: 10.1038/ncomms13663 OPEN

Reconfigurable exciton-plasmon interconversion for nanophotonic circuits

Hyun Seok Lee[1,2], Dinh Hoa Luong[1,2], Min Su Kim[1,2], Youngjo Jin[1,2], Hyun Kim[1,2], Seokjoon Yun[1,2] & Young Hee Lee[1,2]

The recent challenges for improving the operation speed of nanoelectronics have motivated research on manipulating light in on-chip integrated circuits. Hybrid plasmonic waveguides with low-dimensional semiconductors, including quantum dots and quantum wells, are a promising platform for realizing sub-diffraction limited optical components. Meanwhile, two-dimensional transition metal dichalcogenides (TMDs) have received broad interest in optoelectronics owing to tightly bound excitons at room temperature, strong light-matter and exciton-plasmon interactions, available top-down wafer-scale integration, and band-gap tunability. Here, we demonstrate principal functionalities for on-chip optical communications via reconfigurable exciton-plasmon interconversions in ~200-nm-diameter Ag-nanowires overlapping onto TMD transistors. By varying device configurations for each operation purpose, three active components for optical communications are realized: field-effect exciton transistors with a channel length of ~32 μm, field-effect exciton multiplexers transmitting multiple signals through a single NW and electrical detectors of propagating plasmons with a high On/Off ratio of ~190. Our results illustrate the unique merits of two-dimensional semiconductors for constructing reconfigurable device architectures in integrated nanophotonic circuits.

[1] Center for Integrated Nanostructure Physics (CINAP), Institute for Basic Science (IBS), Suwon 440-746, Korea. [2] Department of Energy Science, Sungkyunkwan University, Suwon 440-746, Korea. Correspondence and requests for materials should be addressed to H.S.L. (email: hs.lee@skku.edu) or to Y.H.L. (leeyoung@skku.edu).

Photonics for light manipulation have the potential to meet the recent information technology demands of high-speed and massive data processing[1,2]. Electrical switches, wavelength converters and multiplexers are crucial components for integrating optical circuits[2–6]. Quantum well (QW)-based excitonic transistors, in which exciton flux excited by photons diffuses along the QW channel and switched by the gate modulation of channel potential, are promising devices to realize high-speed interconnections[7,8]. Nevertheless, short-lived excitons and the finite exciton binding energy critically limit the operation to low temperatures within the limited channel length of typically less than 3 μm[7,9]. Moreover, a wavelength conversion, that converts an optical signal to a desired wavelength, and a multiplexing technique, that delivers various signals through a single optical guide, are essential to designing the reconfigurable optical communication systems. Although various methods for the wavelength conversion and multiplexing have been developed in conventional technologies based on fibre optics and photonic waveguides, the optical diffraction limit is a fundamental obstacle to reducing the optical component sizes to nanometers[4–6]. Surface plasmon polaritons (SPPs), which are the electromagnetic waves coherently coupled with electron plasma in metals, have the potential to overcome these issues because they allow a strong localization of optical energy at the metal-dielectric interface at a sub-wavelength scale[4,5,10]. Therefore, the use of metallic nanostructures for plasmonic waveguides allows for light manipulation at a nanoscale[1,2,11].

Meanwhile, recently emerged 2D semiconductors have unique merits for nanophotonics[3,10,12,13]. The absence of dangling bonds allows for various combinations of van der Waal heterostructures[14,15] and adaptability with various substrate choices[16], in contrast with the cumbersome epitaxial growth of QWs in limited substrates and processes[7,8,17,18]. The 2D layered structure of transition metal dichalcogenides (TMDs) offers an easy integration for wafer-scale devices[19] and an efficient electrical tunability of optical-electrical properties[3,13], while the top-down approach for arranging quantum dots (QDs) and injecting electrons to individual QDs for optical modulation are still challenging[20–22]. The bandgap is tunable from visible to infrared range by varying the TMDs, alloying[23] and heterostructures[14], which allows a wide-spectral selectivity[10,12]. The device integration and the electrical modulation of exciton fluxes of 2D semiconductors are easier[24] compared to QDs[22]. Tightly bound excitons of TMDs at room temperature allow for room temperature operable excitonic devices[24], which is a stark contrast to QW-based devices operating at a low temperature[7]. Moreover, the efficient excitons-to-plasmon conversion effects with a conversion efficiency as high as ~32% have been demonstrated in Ag-NW/TMD hybrids[25,26].

Here, we demonstrate the crucial optical components for nanophotonic circuits using reconfigurable exciton-to-plasmon and plasmon-to-exciton interconversions. To realize these concepts, we introduce Ag-nanowires (NWs) for SPP waveguides to 2D semiconductor devices. The Ag-NW waveguides and their

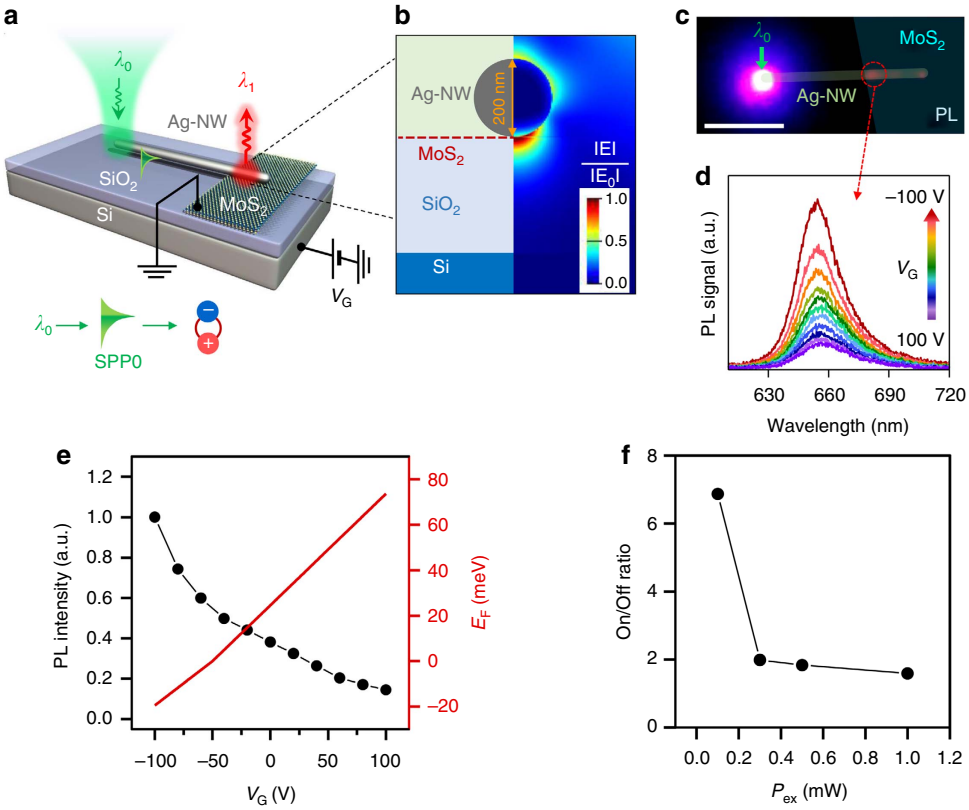

Figure 1 | Photon-plasmon-exciton conversion and exciton flux modulation. (**a**) An Ag-NW overlapped on the monolayer MoS_2 FET. Incident laser (λ_0) at the end of NW is converted to SPP (SPP0). The propagating SPP0 along the NW is absorbed in MoS_2, and the λ_1 exciton is generated at the NW/MoS_2 overlapping region. The λ_1 flux is modulated by V_G. (**b**) Cross-section at the NW/MoS_2 overlapping region and optical field map calculated using an FDTD method, implying optical mode confinement near the NW. (**c**) PL image overlaid with false-coloured MoS_2 flakes and the NW. Scale bar: 5 μm. Green arrow: λ_0 position. Red-dashed circle: PL collection position. (**d**) PL spectra as a function of V_G ranging from −100 V (On state) to 100 V (Off state). (**e**) Integrated PL intensity curve (left axis) and the calculated Fermi level (E_F, right axis) as a function of V_G. (**f**) On/Off ratio of the integrated intensity as a function of laser power (P_{ex}).

hybrids have been well investigated for various purposes because of low ohmic losses and sub-diffraction limited dimensions[2,27,28]. Using Ag-NW-hybridized 2D semiconductor devices with various configurations, three active components for optical communications are realized: field-effect exciton transistors, field-effect exciton multiplexers and electrical detectors of propagating plasmons.

Results

Electrical modulation of plasmon-induced exciton flux. Figure 1a depicts a schematic for the photon-plasmon-exciton conversion process and electrical modulation of the exciton flux. A 200-nm-diameter Ag-NW for SPP waveguides is partially overlapped with a monolayer MoS_2 field-effect transistor (FET) on an SiO_2 (300 nm)/Si wafer. The laser light ($\lambda_0 = 514$ nm) is focused to the left end of the NW and λ_0 is coupled to SPP (SPP0) in the NW[20,26] (see Methods). The SPP0 propagates along the NW in the axial direction with a tightly confined optical near-field[20,26,29] (Fig. 1b). The near-field of SPP0 is absorbed in MoS_2 layers and excites excitons ($\lambda_1 \approx 660$ nm) at the NW/MoS_2 overlapping region[26,30] (see Supplementary Note 1 and Supplementary Fig. 1), where the exciton fluxes are modulated by gate bias (V_G) for excess carrier doping[13,24].

Figure 1c shows the photoluminescence (PL) image overlaid with the sample schematic of the MoS_2 flake and NW, where the green arrow is the λ_0 position and the red-dashed circle indicates the PL collection position. Figure 1d shows the PL spectra as a function of V_G ranging from -100 V (On state) to 100 V (Off state). The PL intensity increases gradually as V_G is reduced. The Fermi level was calculated from the excess electron and hole densities derived from the back-gate capacitance as a function of V_G, as plotted in Fig. 1e, where the charge neutrality point near -50 V is taken as a reference[24] (see Supplementary Note 2 and Supplementary Fig. 2), consistent with the intrinsic n-type doping state in MoS_2. While the Fermi level increases due to the increased electron carriers at high $+V_G$, the PL intensity gradually decreases in proportion to E_F, which is attributed to the Pauli blocking effect for excitons[24]. With increasing n-doping ($V_G > -50$ V), the photoexcited electrons are suppressed by Pauli blocking effect and do not contribute to excitonic emission. Consequently, neutral excitons decrease and negative trions increase. Conversely, with increasing p-doping ($V_G < -50$ V), the Pauli blocking disappears. As a result, both neutral excitons and positive trions increase, and thus, a total exciton flux for p-doping case is larger than that for n-doping case (see Supplementary Fig. 3a). Figure 1f shows an On/Off ratio of exciton fluxes as a function of input laser power (P_{ex}). The On/Off ratio reaches a factor of 7 at $P_{ex} = 0.1$ mW and details are discussed in Supplementary Note 3 and Supplementary Fig. 3.

Exciton transistor via exciton-plasmon interconversions. We demonstrate field-effect exciton transistors with a long channel length (~ 32 μm) via plasmon-to-exciton and exciton-to-plasmon interconversions. Figure 2a depicts the operation principle, where MoS_2-FET is located in the middle of the NW. The SPP0 coupled from λ_0 is absorbed in the MoS_2 layer (as discussed in Fig. 1a) and generate exciton (λ_1). The generated λ_1 is recoupled to SPP1 and propagates along the NW (Fig. 2a). Finally, the SPP1 is converted to λ_1 via scattering at the right end of NW (see Methods). Figure 2b shows an optical micrograph and PL image of the hybrid device. The green arrow is the λ_0 illumination, the red arrow near the NW/MoS_2 overlapping region is the λ_1 emission and the red spot at the right end of the NW (blue-dashed circle) is a PL collection position for Fig. 2c. In the λ_1 emission region, the propagating SPP0 along the NW is converted to SPP1 via exciton-plasmon interconversion and the propagating SPP1 is monitored by the λ_1 scattering at the right end of NW. Clear On ($V_G = -100$ V) and Off ($V_G = 100$ V) states of the PL are displayed in Fig. 2c. Notably, the demonstrated channel length reaches ~ 32 μm at room temperature, ~ 10 times longer that of QW-

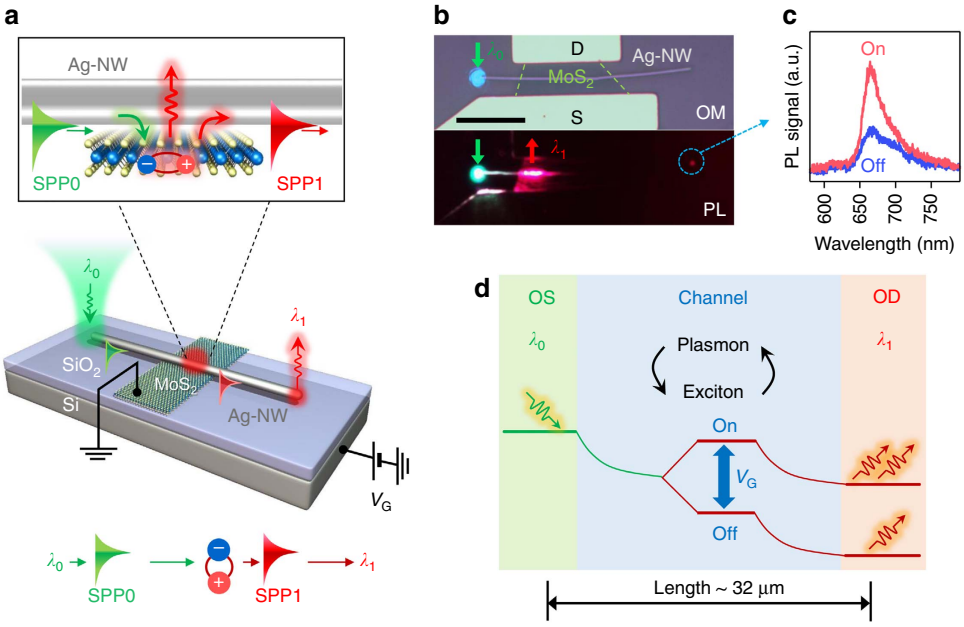

Figure 2 | Long channel exciton transistor. (**a**) A long Ag-NW overlapped on the MoS_2 FET. The incident λ_0 is converted to SPP0. The SPP0 propagating along the NW is absorbed in MoS_2, and the λ_1 exciton is generated at the NW/MoS_2 overlapping region. The λ_1 is recoupled to SPP1 near the NW and scattered out at the right end of the NW. The λ_1 flux is modulated by V_G. (**b**) Optical micrograph overlaid with false-coloured MoS_2 flakes (top) and PL image (bottom) of the exciton transistor. Source (S) and drain (D) for electrodes of the FET. Green arrow: λ_0 position. Red arrow: λ_1 emission. Blue dashed circle: PL collection position. Scale bar: 10 μm. (**c**) PL spectra for On (-100 V) and Off (100 V) states. (**d**) Schematic depicts the transistor operation. Optical source (OS): λ_0 input. Optical drain (OD): λ_1 output. Channel: NW and NW/MoS_2 overlapping region.

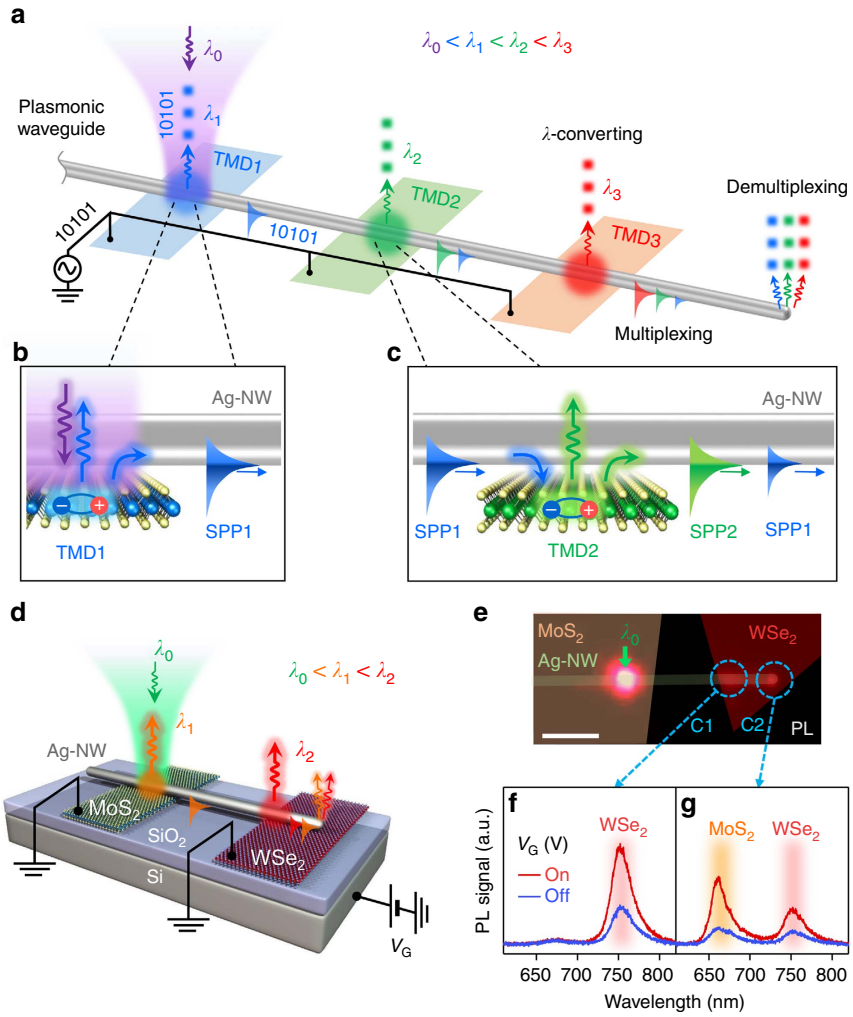

Figure 3 | Exciton multiplexer. (**a**) Laterally arrayed TMDs with different bandgaps bridged via an Ag-NW. The exciton flux of each TMD with the corresponding wavelength (λ) is switched by electrical doping, (**b**) λ_1 excited by the input light is coupled to SPP1 in the NW, (**c**) propagates along the NW and then excites λ_2 by partially being absorbed in TMD2 that is coupled to SPP2 in the NW. SPP1 and SPP2 excite λ_3 in TMD3 and generate SPP3. The three SPP modes deliver the multiplexed wavelengths with optical information generated by electrical modulation. The multiplexed wavelengths are further de-multiplexed by far field scattering at the NW end. (**d**) Schematic of the device consisting of MoS_2 and WSe_2 monolayers bridged by Ag-NW. Each exciton flux is modulated by V_G. (**e**) PL image overlaid with the device structure. The green arrow is the λ_0 position. C1 and C2 are the PL collection positions. Scale bar: 2 μm. The PL spectra measured at (**f**) C1 and (**g**) C2 positions for V_G of −100 and 100 V.

based excitonic transistors (~3 μm) at low temperatures[7,8]. In the Ag-NW, the corresponding 1/*e* SPP propagation lengths are calculated to 12–31 μm for 620–760 nm visible light (see Methods), which quantitatively agrees with our experimental results. Even longer propagation length of ~50 μm at a visible range has been demonstrated in patterned Ag films by the CMOS process on a wafer scale[31]. These length scales are compatible with current nanoelectronics[1]. Moreover, TMDs with smaller bandgaps for long wavelengths can allow even longer SPP propagation. The concept of the field-effect exciton transistor is schematically summarized in Fig. 2d, where the optical source (OS) is the λ_0 input, the optical drain (OD) is the λ_1 output and the channel is the NW and NW/MoS_2 overlapping region.

Reconfigurable exciton-plasmon interconversions. The exciton-plasmon interconversion is more reconfigurable for advanced device architectures. Figure 3a illustrates the operation principle for wavelength multiplexers. Laterally arrayed TMD-FETs, having different bandgaps, are interconnected by an Ag-NW. The excitonic emission wavelength of TMD1, TMD2 and TMD3 corresponds to wavelengths λ_1, λ_2 and λ_3 ($\lambda_1 < \lambda_2 < \lambda_3$), respectively. With the laser (λ_0) incident on the NW/TMD1 overlapping region, the exciton corresponding to λ_1 ($> \lambda_0$) is generated from TMD1. The λ_1 is coupled to SPP1 near the NW (Fig. 3b) without momentum matching via the Förster resonance energy transfer of excitons to plasmons[21,32]. The generated SPP1 propagates along the NW, encounters TMD2 and excites λ_2, which is partially absorbed in TMD2. The similarly generated λ_2 propagates along the NW (Fig. 3c). Likewise, the SPP1 and SPP2 excite λ_3 in TMD3 and generate the SPP3. Eventually, λ_1, λ_2 and λ_3 are multiplexed in the three SPP modes, which are detected at the NW end (see Supplementary Notes 4 and 5 and Supplementary Figs 4 and 5). During this multiplexing process, electrostatic doping of TMD-FETs modulates the exciton fluxes for optical switching information. Notably, the λ_0 is simply converted to multiple wavelengths via sequential exciton-to-plasmon and plasmon-to-exciton interconversion processes, where excitonic wavelengths are determined by the bandgaps of the TMDs.

Figure 3d shows the device structure and experimental setup required to prove such a concept. Monolayer MoS_2 and WSe_2

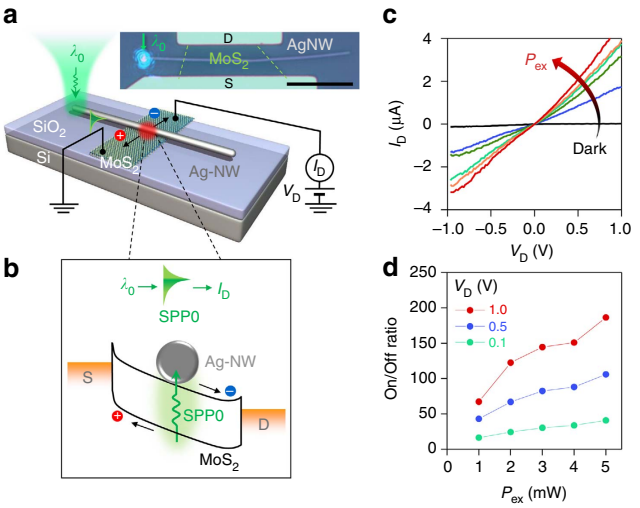

Figure 4 | Electrical detection of plasmons. (**a**) An Ag-NW overlapped on the MoS_2 FET. Incident λ_0 at the end of NW is converted to SPP0. The propagating SPP0 along the NW is absorbed in MoS_2 and converted to photocurrent (I_D) at the NW/MoS_2 overlapping region. Scale bar: 10 μm. (**b**) Schematic description of photocurrent generation via plasmon-to-charge conversion at the NW/MoS_2 overlapping region. (**c**) I_D-V_D curves of MoS_2 FET for various P_{ex} ranging from 1 to 5 mW. Black curve: laser-off state (Dark). (**d**) On/Off ratio as a function of P_{ex} for the selected V_D from (**c**).

FETs on SiO_2 (300 nm)/Si wafers are interconnected by an Ag-NW. Under the λ_0 illumination on the NW/MoS_2 overlapping region, the generated MoS_2 excitons ($\lambda_1 \approx 660$ nm)[24] are coupled to the SPP1. The SPP1 propagates along the NW and excites the WSe_2 excitons ($\lambda_2 \approx 760$ nm)[33] at the NW/WSe_2 overlapping region (red spot in Fig. 3d) and simultaneously, λ_2 is recoupled to SPP2. Finally, the SPP1 and SPP2 are multiplexed through the single NW. Figure 3e shows PL image overlaid with the sample image of the TMD flakes and the NW, where C1 and C2 indicate the PL signal collection positions. Figure 3f,g shows the PL spectra that are modulated by V_G. The PL spectra for λ_1 and λ_2 are clearly observed at C2 (the NW end) via individual plasmon-to-photon conversions from SPP1 and SPP2 to λ_1 and λ_2, implying the wavelength de-multiplexing. The λ_1 scattering at C1 (the NW mid-section) is negligible because the SPP1 is not converted to λ_1 without a scattering source at the NW mid-section (see Methods). Various combinations of wavelengths are available by rearranging the TMD array and vertical stacking (see Supplementary Notes 4–6 and Supplementary Figs 4–6). In addition, the 2D material dependence on the exciton-plasmon interconversion efficiency was not appreciable, while the strength of the exciton-plasmon interaction strongly relies on the exciton quantum yield of each material (see Supplementary Note 7 and Supplementary Fig. 7). We also investigated the polarization effect of light illumination. A parallel polarization of incident light to an SPP propagation direction along the Ag-NW is essential for the exciton-plasmon interconversions (see Supplementary Note 8 and Supplementary Fig. 8).

Electrical detection of plasmons with high On/Off ratios. The propagating plasmons are also detectable by electrical signals, which is another key component for nanophotonic circuits. Figure 4a shows the device structure and experimental setup to prove such a concept using the device for Fig. 2. The SPP0 generated by λ_0 is absorbed in the MoS_2 layer (as discussed in Figs 1 and 2). The absorbed SPP0 generates electron-hole pairs which are separated to a plasmonic photocurrent via plasmon-to-charge conversion[30,34] under an applied drain bias at the MoS_2 FET (Fig. 4b). Figure 4c shows I_D-V_D curves of the Ag-NW overlapped MoS_2 FET for a dark state and under λ_0 illuminations at the NW end with various P_{ex}. The SPP0 induced photocurrents (for On state) are two orders of magnitude higher than the dark current (Off state). The photocurrent increases with V_D because of an increased drift velocity of photocarriers and a reduced carrier transit time[35]. Figure 4d shows On/Off ratios of I_D in proportion to P_{ex} for various V_D. The maximum On/Off ratio reaches ~ 190 for $P_{ex} = 5$ mW and $V_D = 1$ V.

Discussion

In summary, we have demonstrated the crucial optical components for nanophotonic circuits using the reconfigurable exciton-plasmon interconversion and efficient exciton flux modulation of TMDs in various Ag-NW/TMD hybrid architectures at room temperature. The exciton transistor was realized by partially overlapping the Ag-NW on TMD-FETs. The laser-coupled-plasmon propagates through the Ag-NW channel and sequentially excites excitons of TMD-FETs where the exciton flux was modulated by electrical gate doping. Wavelength multiplexing devices were realized by interconnecting Ag-NW to laterally arrayed TMD-FETs having different bandgaps via the sequential exciton-plasmon interconversions. The electrical detections of propagating plasmons along the Ag-NW with a high On/Off ratio were also realized in the Ag-NW hybridized TMD-FET. Our demonstrations of the reconfigurable exciton-plasmon interconversions in various device architectures pave a way to realize various optical components for nanophotonic integrated circuits having advantages of adaptability in wavelength selection and scalability.

Methods

Sample preparation. The MoS_2, WS_2 and WSe_2 monolayer flakes were synthesized on an SiO_2 (300 nm)/Si substrate using a chemical vapour deposition method[36]. The synthesized monolayer TMD flakes were transferred onto an SiO_2 (300 nm)/Si wafer via the conventional poly(methyl methacrylate) (PMMA) support method[36]. The Ag-NW with a diameter of ~ 200 nm (PlasmaChem Corp.; dispersed in isopropyl alcohol) was transferred onto the flake-transferred samples and dried under ambient conditions. The electrical contacts to the TMDs were fabricated by the metal evaporation of Cr/Au (10/50 nm) and e-beam lithography patterning method, where an Si wafer was used to apply the back-gate bias. Finally, the samples were covered with a ~ 400-nm-thick PMMA (950 K PMMA, MicroChem Corp., 4% in chlorobenzene) layer to protect the NW from degradation under ambient conditions[25].

Characterization. The $I_D - V_G$ measurements in the MoS_2-FET were performed at $V_D = 1$ V using an electrical characterization system (Kiethley 4200-SCS, Kiethley Instruments). The PL spectra under the V_G application (Kiethley 6487 picometer/voltage source, Kiethley Instruments) to the Si substrate and the photocurrents generated by plasmons (Agilent B2902A, Agilent Technologies) were measured at room temperature by using a lab-constructed confocal microscope. A laser beam with a wavelength of 514 nm was focused on the sample using an objective lens ($\times 100$, numerical aperture, 0.9). The PL spectra at the desired positions were collected using a pinhole detector under the illumination of the focused laser at other positions, where the laser beam and pinhole positions were controlled by a micromanipulator. The spectra were recorded using a spectrometer and a cooled charge-coupled device camera[25].

SPP propagation length analysis. SPP modes for the configuration of PMMA/Ag-NW on an SiO_2 (300 nm)/Si substrate were analysed using a finite-difference time-domain numerical simulation (Lumerical Solutions, Inc.) method. The $1/e$ SPP propagation lengths were derived as a function of wavelength from the lowest loss mode among the possible confined modes near the NW[25,26].

Coupling and decoupling of SPPs at distal ends of Ag-NWs. To couple the SPP waveguide modes along the Ag-NW axis by the light illumination, the momentum mismatch for longitudinal mode between the SPPs and the incoming photons should be compensated[29,37]. The light scattering can be used to provide additional

wavevectors. When the focused laser light is illuminated at the midsection of the NWs, a cylindrically symmetric shape of the NWs cannot provide the light scattering in the axial direction, and thus, the activation of the SPP waveguide modes along the NW is negligible. However, when light is illuminated at the end of the NW, the light scattering provides additional wavevectors in all directions because the symmetric shape is broken at the distal edge of the NWs. Therefore, the momentum mismatch between the SPPs and the photons is compensated. As a result, the SPP waveguide modes can be activated. In the reverse process, when the propagating SPP modes face the distal end of the NWs, the SPPs are decoupled to radiative emissions but not at the NW midsection[29,37].

Data availability. The data that support the findings of this study are available from the corresponding authors H.S.L and Y.H.L on request.

References

1. Ozbay, E. Plasmonics: merging photonics and electronics at nanoscale dimensions. *Science* **311,** 189–193 (2006).
2. Fang, Y. R. & Sun, M. T. Nanoplasmonic waveguides: towards applications in integrated nanophotonic circuits. *Light-Sci. Appl.* **4,** e294 (2015).
3. Sun, Z. P., Martinez, A. & Wang, F. Optical modulators with 2D layered materials. *Nat. Photonics* **10,** 227–238 (2016).
4. Bozinovic, N. *et al.* Terabit-scale orbital angular momentum mode division multiplexing in fibers. *Science* **340,** 1545–1548 (2013).
5. Dai, D. X. & Bowers, J. E. Silicon-based on-chip multiplexing technologies and devices for Peta-bit optical interconnects. *Nanophotonics* **3,** 283–311 (2014).
6. Ishikawa, H., Watanabe, S. & Kuwatsuka, H. Wavelength conversion technologies for photonic network systems. *Fujitsu Sci. Tech. J.* **35,** 126–138 (1999).
7. High, A. A., Novitskaya, E. E., Butov, L. V., Hanson, M. & Gossard, A. C. Control of exciton fluxes in an excitonic integrated circuit. *Science* **321,** 229–231 (2008).
8. Grosso, G. *et al.* Excitonic switches operating at around 100 K. *Nat. Photonics* **3,** 577–580 (2009).
9. Baldo, M. & Stojanovic, V. Excitonic interconnects. *Nat. Photonics* **3,** 558–560 (2009).
10. Castellanos-Gomez, A. Why all the fuss about 2D semiconductors? *Nat. Photonics* **10,** 202–204 (2016).
11. Gramotnev, D. K. & Bozhevolnyi, S. I. Plasmonics beyond the diffraction limit. *Nat. Photonics* **4,** 83–91 (2010).
12. Xia, F. N., Wang, H., Xiao, D., Dubey, M. & Ramasubramaniam, A. Two-dimensional material nanophotonics. *Nat. Photonics* **8,** 899–907 (2014).
13. Mak, K. F. & Shan, J. Photonics and optoelectronics of 2D semiconductor transition metal dichalcogenides. *Nat. Photonics* **10,** 216–226 (2016).
14. Lee, C. H. *et al.* Atomically thin p-n junctions with van der Waals heterointerfaces. *Nat. Nanotechnol.* **9,** 676–681 (2014).
15. Jin, Y. *et al.* A Van Der Waals homojunction: ideal p-n diode behavior in $MoSe_2$. *Adv. Mater.* **27,** 5534–5540 (2015).
16. Akinwande, D., Petrone, N. & Hone, J. Two-dimensional flexible nanoelectronics. *Nat. Commun.* **5,** 5678 (2014).
17. Huang, K. C. Y. *et al.* Electrically driven subwavelength optical nanocircuits. *Nat. Photonics* **8,** 244–249 (2014).
18. Li, Z. C. *et al.* Suppression of thermal degradation of InGaN/GaN quantum wells in green laser diode structures during the epitaxial growth. *Appl. Phys. Lett.* **103,** 152109 (2013).
19. Kang, K. *et al.* High-mobility three-atom-thick semiconducting films with wafer-scale homogeneity. *Nature* **520,** 656–660 (2015).
20. Akimov, A. V. *et al.* Generation of single optical plasmons in metallic nanowires coupled to quantum dots. *Nature* **450,** 402–406 (2007).
21. Miyata, M. & Takahara, J. Colloidal quantum dot-based plasmon emitters with planar integration and long-range guiding. *Opt. Express* **21,** 7882–7890 (2013).
22. Shirasaki, Y., Supran, G. J., Bawendi, M. G. & Bulovic, V. Emergence of colloidal quantum-dot light-emitting technologies. *Nat. Photonics* **7,** 13–23 (2013).
23. Mann, J. *et al.* 2-dimensional transition metal dichalcogenides with tunable direct band gaps: $MoS_{2(1-x)}Se_{2x}$ monolayers. *Adv. Mater.* **26,** 1399–1404 (2014).
24. Lee, H. S., Kim, M. S., Kim, H. & Lee, Y. H. Identifying multiexcitons in MoS_2 monolayers at room temperature. *Phys. Rev. B* **93,** 140409(R) (2016).
25. Lee, H. S. *et al.* Selective amplification of the primary exciton in a MoS_2 monolayer. *Phys. Rev. Lett.* **115,** 226801 (2015).
26. Lee, H. S. *et al.* Efficient exciton-plasmon conversion in Ag nanowire/monolayer MoS_2 hybrids: direct imaging and quantitative estimation of plasmon coupling and propagation. *Adv. Opt. Mater.* **3,** 943–947 (2015).
27. Huang, Y. Z., Fang, Y. R., Zhang, Z. L., Zhu, L. & Sun, M. T. Nanowire-supported plasmonic waveguide for remote excitation of surface-enhanced Raman scattering. *Light-Sci. Appl.* **3,** e199 (2014).
28. Sun, M. T. *et al.* Remotely excited Raman optical activity using chiral plasmon propagation in Ag nanowires. *Light-Sci. Appl.* **2,** e112 (2013).
29. Guo, X., Ma, Y. G., Wang, Y. P. & Tong, L. M. Nanowire plasmonic waveguides, circuits and devices. *Laser Photonics Rev.* **7,** 855–881 (2013).
30. Goodfellow, K. M., Chakraborty, C., Beams, R., Novotny, L. & Vamiyakas, A. N. Direct on-chip optical plasmon detection with an atomically thin semiconductor. *Nano. Lett.* **15,** 5477–5481 (2015).
31. Nagpal, P., Lindquist, N. C., Oh, S. H. & Norris, D. J. Ultrasmooth patterned metals for plasmonics and metamaterials. *Science* **325,** 594–597 (2009).
32. Jia, C. *et al.* Interface-engineered plasmonics in metal/semiconductor heterostructures. *Adv. Energy Mater.* **6,** 1600431 (2016).
33. He, K. L. *et al.* Tightly bound excitons in monolayer WSe_2. *Phys. Rev. Lett.* **113,** 026803 (2014).
34. Falk, A. L. *et al.* Near-field electrical detection of optical plasmons and single-plasmon sources. *Nat. Phys.* **5,** 475–479 (2009).
35. Lopez-Sanchez, O., Lembke, D., Kayci, M., Radenovic, A. & Kis, A. Ultrasensitive photodetectors based on monolayer MoS_2. *Nat. Nanotechnol.* **8,** 497–501 (2013).
36. Jeong, H. Y. *et al.* Visualizing point defects in transition-metal dichalcogenides using optical microscopy. *Acs Nano* **10,** 770–777 (2016).
37. Sanders, A. W. *et al.* Observation of plasmon propagation, redirection, and fan-out in silver nanowires. *Nano Lett.* **6,** 1822–1826 (2006).

Acknowledgements

This work was supported by the Institute for Basic Science of Korea (IBS-R011-D1).

Author contributions

H.S.L. designed and developed the work. H.S.L., D.H.L, Y.J., H.K. and S.Y. prepared the samples. H.S.L., D.H.L., M.S.K. and Y.J. performed experiments. H.S.L conducted the numerical simulations. All authors discussed the results. H.S.L. and Y.H.L. analysed and wrote the manuscript.

Additional information

Supplementary Information accompanies this paper at http://www.nature.com/naturecommunications

Competing financial interests: The authors declare no competing financial interests.

Reprints and permission information is available at http://npg.nature.com/reprintsandpermissions/

How to cite this article: Lee H. S., *et al.* Reconfigurable exciton-plasmon interconversion for nanophotonic circuits. *Nat. Commun.* 7, 13663 doi: 10.1038/ncomms13663 (2016).

Publisher's note: Springer Nature remains neutral with regard to jurisdictional claims in published maps and institutional affiliations.

This work is licensed under a Creative Commons Attribution 4.0 International License. The images or other third party material in this article are included in the article's Creative Commons license, unless indicated otherwise in the credit line; if the material is not included under the Creative Commons license, users will need to obtain permission from the license holder to reproduce the material. To view a copy of this license, visit http://creativecommons.org/licenses/by/4.0/

© The Author(s) 2016